

Phase transformation as the mechanism of mechanical deformation of vertically aligned carbon nanotube arrays: Insights from mesoscopic modeling

Bernard K. Wittmaack^a, Alexey N. Volkov^b, Leonid V. Zhigilei^{a,*}

^a Department of Materials Science and Engineering, University of Virginia, 395 McCormick Road, Charlottesville, VA, 22904-4745, USA

^b Department of Mechanical Engineering, University of Alabama, H. M. Comer Hall, 7th Avenue, Tuscaloosa, AL, 35487, USA

ARTICLE INFO

Article history:

Received 17 October 2018

Received in revised form

19 November 2018

Accepted 20 November 2018

Available online 21 November 2018

ABSTRACT

Vertically aligned carbon nanotube (VACNT) arrays or “forests” behave mechanically as foams when compressed, exhibiting a characteristic nonlinear stress – strain response. However, the fiber structure of VACNT forests is unlike that of cellular foams, and the microscopic mechanisms of the deformation are quite different. While numerous studies have addressed the mechanical response of VACNT forests undergoing uniaxial compression, the underlying deformation mechanisms are not yet fully established. In this paper, we report the results of large-scale mesoscopic simulations of the uniaxial compression of a VACNT forest composed of 2- μm -long carbon nanotubes (CNTs) as well as three structurally distinct forests composed of 0.6- μm -long CNTs. The simulations reveal that the compressive deformation proceeds as a phase transformation from an original low-density phase composed of vertically aligned CNT bundles to a densified phase with horizontal alignment of CNTs. The two phases are separated by a well-defined interfacial layer, which advances during the compressive deformation through localized bending and folding of nanotubes. For the 2- μm -tall forest, the folding involves correlated displacements of multiple CNT bundles, hinting on the origin of the collective buckling behavior observed in experiments. The characteristic three-stage stress-strain dependence (an initial “elastic” peak followed by an extended plateau region and a sharp rise of stress in the densification regime), commonly observed in experimental probing of the mechanical properties of VACNT forests, is reproduced in all of the simulations, suggesting that the heterogeneous propagation of densification front may be the general mechanism of the mechanical deformation of VACNT forests.

© 2018 Elsevier Ltd. All rights reserved.

1. Introduction

The mechanical response of vertically aligned carbon nanotube (VACNT) forests [1] to compression is comparable to that of cellular foams [2]. In particular, similar to foams, VACNT forests can undergo repeated loading to high strains while maintaining their resilience [3–5] and exhibit a three-stage stress – strain response [6–8] consisting of (1) an elastic regime where the bending and stretching deformations of CNT bundles do not involve any significant structural changes in the material and stress increases linearly with strain, (2) an extended plateau regime characterized by relatively weak stress dependence on strain and structural

rearrangements that do not lead to significant strengthening, and (3) a densification regime where the reorganization within the material becomes spatially constrained, leading to a rapid increase in stress. Despite the similarity of the mechanical behavior, the deformation mechanisms of VACNTs forests and foams are rather different. Foams deform either through bending-dominated mechanisms where cell walls bend and buckle or by stretching-dominated processes where the struts supporting the cell walls are loaded axially [2,9]. These deformation mechanisms, however, are not applicable to VACNT forests, which are structurally characterized as anisotropic networks of interconnected CNT bundles, quite unlike the cellular motif common to conventional foams.

The complex multi-stage stress – strain dependence of VACNTs undergoing uniaxial compression is commonly attributed to the coordinated, localized buckling of bundles of CNTs occurring periodically along the height of the forest [3,4,6,10–12]. Specifically,

* Corresponding author.

E-mail address: lz2n@virginia.edu (L.V. Zhigilei).

heterogeneity in the density and nanotube alignment in nanotube forests results in preferential nucleation sites for coordinated buckling of CNTs at relatively compliant sections [3,6,13–15], forming localized high-density regions at the locations of buckling. Analytically, the non-linear, multi-stage stress – strain response of VACNT forests has been described [13,16–18] by representing CNT as a series of bi-stable springs [19–21] which are characterized by an energy landscape with two minima separated by a convex "spinodal" region. The energy minima correspond to low and high strain conformations of the spring, and when many springs are connected in series the mechanical response is similar to that of a CNT undergoing compression. The bi-stable spring model saw success in reproducing the characteristic three-stage stress – strain curve of uniaxially compressed forests [16,18]. In the latest of these reports [18], the interpretation of the deformation behavior of VACNT forests in terms of a phase transition between a rarefied phase, in which the CNTs are mostly vertically aligned, and a densified phase stabilized by the inter-tube van der Waals interactions is suggested. This hypothesis was partially motivated by earlier studies of biopolymer (fibrin) network structures exhibiting three-stage stress response to the uniaxial compression, similar to that of foams and VACNT forests [22,23], and deforming by separation into two distinct, coexisting low- and high-density phases. Moreover, the formation of localized densified regions during uniaxial compression has also been observed for VACNT forests [3,6–8,24].

Despite the extensive experimental and modeling efforts, and the success of the bi-stable spring model in reproducing the phase coexistence and stress – strain response of VACNT forests undergoing compression, the structural characteristics of the two phases and the mechanisms of the phase separation remain elusive. Major obstacles to a systematic analysis of the mechanisms of mechanical deformation of VACNT forests come from the challenge of growing forests with precisely controllable structure, as well as the difficulty of detailed characterization of the structural and energetic parameters of VACNT forests undergoing compression. Computationally reproducing the structure of VACNT forests and inspecting the structural transformations in the course of mechanical deformation is one way to circumvent the problem of detailed structural characterization of experimental samples. The emergence of a new class of coarse-grained mesoscopic models for mesoscopic dynamic simulation of large groups of CNTs [25–28], combined with a recent development of an effective method for the generation of computational samples with tunable microstructures based on self-organization of nanotubes into anisotropic network structures [29], have enabled realistic modeling of the mechanical deformation of VACNT forests.

First mesoscopic simulations of the uniaxial compression of short VACNT forests [8] have indeed demonstrated the ability of the mesoscopic modeling to reproduce the three-stage stress – strain dependence characteristic of experimental samples and provided initial insights into the dependence of the mechanical behavior of VACNT forests on density, microstructure (bundle size distribution and degree of nanotube alignment), loading rate, and interaction with the indenter. The 0.2- μm -tall forests used in these first simulations, however, are too short for reproducing the periodic coordinated buckling across the sample and testing the hypothesis on the coexistence of low- and high-density phases suggested for interpretation of experimental observations [6,7,10,14,18,24].

In this paper, we report the results of mesoscopic simulations of VACNT forests consisting of longer, 0.6- μm - and 2- μm -long, nanotubes, and focus our attention on the mechanisms of the phase transformation occurring in the course of the mechanical deformation of the CNT network materials and the nature of the two phases produced by the deformation. The dynamic mesoscopic

model, the structural characteristics of *in silico* VACNT forest samples, and the computational setup for simulation of uniaxial compression of the samples are briefly described below, in section 2. The detailed analysis of the phase separation in a 2- μm -tall VACNT forest undergoing uniaxial compressive deformation is provided in section 3. The effect of the microstructure on the mechanical response of VACNT forests is explored in a series of simulations performed for 0.6- μm -tall forests and reported in section 4. Finally, the main conclusions of this computational study are summarized in section 5.

2. Computational model

2.1. Mesoscopic force field model for carbon nanotube materials

The mesoscopic force field model developed for realistic large-scale simulations of CNT materials is based on a coarse-grained representation of individual CNTs as chains of stretchable cylindrical segments [25,26]. The state of each segment is defined by positions, velocities, and the internal temperature of nodes joining the neighboring segments [25]. The dynamics of a system of interacting CNTs is described by solving the equations of motion of classical mechanics for the positions of all nodes [25]. The forces acting on the nodes are calculated based on the mesoscopic force field that accounts for stretching and bending deformation of individual CNTs [25], bending buckling of CNTs [30], as well as for the van der Waals inter-tube interactions [26], with all terms of the force field parameterized based on the results of atomistic simulations. The possibility of both axial and bending fracture of individual CNTs is included in the model, where either event results in clean CNT fragmentation. For (10,10) single-walled carbon nanotubes (SWCNTs), the axial fracture is set to occur at a local strain of 0.279 [31], and the bending fracture occurs at a local bending angle of 120° [32]. In the simulations reported in the present paper, only the bending fracture is observed in some of the nanotubes at the late stage of the VACNT forest compression, but it does not significantly affect the overall mechanical response of the forests (see Fig. S1 in the Supplementary Data). The mesoscopic force field does not include an explicit description of friction forces related to the relative displacement of tubes with respect to each other, as these forces are too weak to prevent room-temperature rearrangements of defect-free CNTs [33,34]. The contribution of interfacial sliding forces originating from changes in the inter-tube van der Waals interaction area, however, is fully accounted for in the mesoscopic model, and, in the case of pristine CNTs, is substantially larger than the static and dynamic friction forces related to the atomic corrugation of the interaction between the nanotube surfaces [35,36]. The presence of defects, functional groups, and chemical cross-links can significantly increase the strength of the shear interactions between nanotubes [37,38], but these effects are not considered in the present study.

2.2. VACNT forest samples

A series of morphologically diverse computational samples with realistic structural organization is generated *in silico* following the procedure outlined in Ref. [29]. Briefly, the procedure is as follows. First, full-length straight CNTs are positioned randomly on a substrate until a prescribed tube density is reached. Each CNT is given a random inclination angle with respect to the vertical axis, falling between zero and a specified maximum inclination, Θ_{max} , with uniform probability. Then, the initial sample undergoes thermal annealing in a mesoscopic dynamic simulation performed at a temperature of 5,000 K for 1 ns (the model does not include the possibility of thermal decomposition of CNTs, and the temperature

is defined based on the average kinetic energy of mesoscopic dynamic units of the model). In the course of the thermal annealing, the initially straight and isolated nanotubes self-organize into a continuous network of bundles with the bundle size distribution largely defined by the material density and Θ_{max} [29]. Finally, the computational VACNT forest is quenched to 300 K and allowed to relax until a metastable configuration, defined as a state where the rate of change in inter-tube interaction energy slows down to a level below 0.05% per ns, is obtained.

All samples considered in this work consist of (10, 10) SWCNTs with a radius of 0.6785 nm and have a mass density of 0.02 g/cm³ (areal density of 6.09×10^{11} CNT/cm²). The density of the VACNT forest samples falls well within the range of CVD grown samples [39–43], and assigning a uniform radius to every CNT within the forest is a good approximation for the tightly distributed radii of SWCNTs [44]. The tallest sample used in the simulation discussed in section 3 consists of 2,498 2- μ m-long CNTs on a $0.64 \times 0.64 \mu\text{m}^2$ substrate and is designated as sample FA. The structure of this sample is illustrated in Fig. S2a in the Supplementary Data). With each internal node (dynamic unit in the mesoscopic model) representing a 2-nm-long segment of a nanotube, the computational sample is composed of 2,500,498 nodes.

Three smaller samples, consisting of 0.6- μ m-long CNTs randomly distributed on a $0.60 \times 0.60 \mu\text{m}^2$ substrate, are referred to as samples FB, FC, and FD (see Figs. S2b–d in the Supplementary Data). These samples are generated with different values of Θ_{max} and are used for investigation of the structural dependence of the mechanical behavior of VACNT forests reported in section 4. In all simulations, the periodic boundary conditions are applied in the lateral directions (parallel to the surface of the substrate), thus effectively representing VACNT forests extending much further than the actual lateral dimensions of the computational systems.

The structure of the *in silico* samples is characterized by calculating a set of parameters listed in Table 1, including the average tilt of CNT segments with respect to the direction of VACNT alignment $\langle \theta \rangle$, average bundle size $\langle N_B \rangle$, maximum bundle size N_B^{max} , standard deviation (SD) of the bundle size, and magnitude of the Herman orientation factor (HOF) defined as $S = \frac{1}{2}[3\langle \cos \theta \rangle - 1]$, where θ is the local angle between a nanotube and the vertical axis, and the angled brackets $\langle \rangle$ denote averaging over the CNT segments. The HOF quantifies the extent of the orientation of nanotubes with respect to the vertical axis and ranges from -0.5 to 1 , where values of -0.5 , 0 , and 1 correspond to perpendicular alignment, random orientation, and parallel alignment with respect to the axis, respectively.

Among the 0.6- μ m-tall forests, sample FB is prepared with the smallest Θ_{max} of 0.6° and has highly vertically oriented, thick CNT bundles with a relatively low degree of interconnection between the bundles. Sample FD is prepared with the largest Θ_{max} of 27° , is poorly aligned (lowest HOF), and features thinner bundles organized into a more complex, entangled network. Sample FC is

prepared with Θ_{max} of 12° and features structural characteristics intermediate between FB and FD samples (Table 1). The tallest VACNT forest FA is prepared with the same Θ_{max} as sample FC and has a similar degree of alignment, as characterized by $\langle \theta \rangle$ and HOF. The average and maximum bundle sizes, however, are substantially larger in the tall forest, reflecting the reduced influence of the constraints related to the attachment of nanotubes to the substrate and the increased freedom of the nanotubes to join multiple bundles across the height of the forest.

2.3. Simulation of the uniaxial compression

The uniaxial compression of VACNT forests is simulated with a rigid planar indenter spanning the entire top surface of the sample and interacting with CNTs via a purely repulsive potential. The repulsive potential between the indenter and a part of a CNT represented by node i is defined by an inverse-power-law function $\epsilon m_i \left(\frac{\sigma}{\Delta z_i - R_T} \right) S(\Delta z_i - R_T)$, where Δz_i is the distance between the surface of the indenter and the CNT node i , R_T is the radius of the nanotube, m_i is the mass associated with mesoscopic node i , and $S(\Delta z_i - R_T)$ is a cubic spline function providing smooth cutoff of the potential in the range of $10 \text{ \AA} \leq \Delta z_i - R_T \leq 12 \text{ \AA}$. The parameters of the potential function, $\epsilon = 0.254 \times 10^{-3}$ eV/Da and $\sigma = 3.6 \text{ \AA}$, are chosen to roughly represent the repulsive part of the non-bonded interaction potential between a graphene sheet and a nanotube aligned along the graphene. The shape of the repulsive potential is sufficiently steep to ensure that only the nanotubes that are in direct contact with the indenter are experiencing repulsive forces from the indenter. Since the repulsive force produced by the potential acts only in the direction normal to the indenter surface, the interaction with indenter does not introduce any tangential friction forces and does not directly constrain the CNT motion along the indenter surface.

The indenter velocity of 50 m/s, corresponding to deformation rates of $8.3 \times 10^7 \text{ s}^{-1}$ and $2.5 \times 10^7 \text{ s}^{-1}$ for the 0.6- μ m- and 2- μ m-tall forests, respectively, is used in the simulations. While the indenter velocity of 50 m/s is much higher than typical experimental values of 1–1,000 nm/s, matching the deformation rates used in experiments is computationally impractical. For instance, for sample FA consisting of over 2.5 million nodes, the compression to 0.9 engineering strain at the indenter velocity of 50 m/s takes 36 ns and requires 0.9 M CPU hours on the *Comet* supercomputer [45]. The stress – strain curves predicted in earlier simulations of the uniaxial compression of shorter VACNT forests consisting of 0.2- μ m-long CNTs [8], are found to be in a semi-quantitative agreement with those reported in experimental studies, despite the high deformation rates of 5×10^7 to $2.5 \times 10^8 \text{ s}^{-1}$ used in the simulations. Moreover, only moderate quantitative changes in the stress – strain response are observed upon a decrease of the deformation rate from 10^8 to $5 \times 10^7 \text{ s}^{-1}$, suggesting that the physical mechanisms of the VACNT deformation are unlikely to change upon further reduction of the deformation rate.

The compression is simulated at a constant temperature of 300 K enforced by the Berendsen thermostat algorithm [46] applied to the coarse-grained units of the model, *i.e.*, the thermal equilibrium between different vibrational models of the system is assumed at all times. The reported stresses are calculated from the total force that the VACNT forest exerts on the indenter. The engineering strain is defined with respect to the length of the CNTs within the forest (*i.e.*, 2 or 0.6 μ m), rather than the maximum initial forest height, which is shorter than the length of the CNTs by less than 1%. For the convenience of representation of stress – strain dependences for VACNT forests undergoing compressive loading, we adopt a sign convention where the stress is positive in compression and present the magnitude of the engineering strain

Table 1

Statistical information on structural parameters of four computational forests of the same density of 0.02 g/cm³ and composed of CNTs with lengths L_{CNT} of 2 and 0.6 μ m. The average tilt of CNT segments $\langle \theta \rangle$, average bundle size $\langle N_B \rangle$, maximum bundle size N_B^{max} , standard deviation (SD) of the bundle size, and magnitude of the Herman orientation factor (HOF) are listed for the computational samples generated at maximum initial inclination angles Θ_{max} of 0.6° , 12° , and 27° .

Sample	L_{CNT}	Θ_{max}	$\langle \theta \rangle$	$\langle N_B \rangle$	N_B^{max}	SD	HOF
FA	2 μ m	12°	17.6°	42	163	28	0.82
FB	0.6 μ m	0.6°	5.7°	28	82	19	0.95
FC	0.6 μ m	12°	17.2°	22	98	18	0.82
FD	0.6 μ m	27°	22.9°	10	65	9	0.72

as a positive quantity.

3. Deformation mechanisms and phase separation in 2- μm -tall VACNT forest

The structural changes produced by the uniaxial compression of sample FA, composed of 2- μm -long CNTs, are discussed herein based on the visual inspection of a series of snapshots taken at different stages of the compressive deformation, as well as quantitative analysis of the evolution of the structural characteristics of the VACNT forests during the deformation. The snapshots of the microstructure are shown in Fig. 1 for the original sample and for four values of the compressive engineering strain. The CNT segments in the snapshots are colored by the local value of the intertube interaction energy using a two-tone coloring scale so that isolated CNT segments and the ones with a small number of neighboring segments are colored red, while the lower-energy segments of bundled nanotubes are colored blue.

The most striking characteristic of the deformation process apparent from the visual inspection of the snapshots is the formation of a densified layer of material near the indenter. Although some bending and coarsening of CNT bundles is observed throughout the thickness of the VACNT forest at the early stage of the deformation, to the engineering strain of 0.2, the structural changes in the lower part of the sample remain rather limited upon further compression, and the most prominent result of the deformation is the thickening of the dense layer in the top part of the forest with increasing compressive strain. Visually, the top dense layer is characterized by the predominantly horizontal orientation of the nanotubes and looks quite distinct from the lower portion of the forest with vertical alignment of the CNT bundles. The appearance of densified layers during compressive deformation has been observed experimentally [3,6,14,18,24], although the details of their structural organization and the formation mechanisms are not yet fully understood. The analysis of the results of the mesoscopic simulations, which provide complete information on the

structural rearrangement leading to the dense layer formation, enables us to address the long-standing question of the mechanism of the heterogeneous deformation behavior of the VACNT forests.

A more detailed picture of the formation of the top dense layer and its structural evolution during the deformation of the VACNT sample is provided by the top-down views of the upper half of the sample shown in Fig. 2. From the snapshots, we see that the CNT bundles in the top part of the sample reorient themselves parallel to the indenter, coarsen by merging with other bundles, and curve into loops to accommodate the increasing crowding in the dense layer. At some point, the rearrangement of the curved, coarse bundles of nanotubes is jammed by the interaction with each other, and the structural evolution in the top layer ceases. Further compressive deformation is then largely accommodated by thickening of the densified layer, which proceeds through the downward propagation of a relatively well-defined interface separating the dense part of the forest composed of curved thick nanotube bundles mostly oriented horizontally (parallel to the substrate) from the rarified part of the forest where the nanotube bundles largely retain their original vertical orientation, Fig. 1.

The visual picture of the compressive deformation described above is consistent with a notion of a phase transformation proceeding through the propagation of the interface that separates the low- and high-density parts of the sample. The degree of the densification and realignment of nanotubes upon this phase transformation can be quantified by tracking the evolution of the local density and orientation of nanotube segments throughout the compression of the sample. Two contour plots for the mass density and CNT orientation (described by local HOF) are shown in Fig. 3. These plots are prepared by partitioning the original, unstrained forest sample into 50 horizontal layers and assigning each CNT segment to a particular layer. Even though the segments are displaced in the course of the compression, the properties of interest are still calculated by averaging over the same set of the segments that were originally located in the same layer. Due to the large difference in density between the two phases generated in the

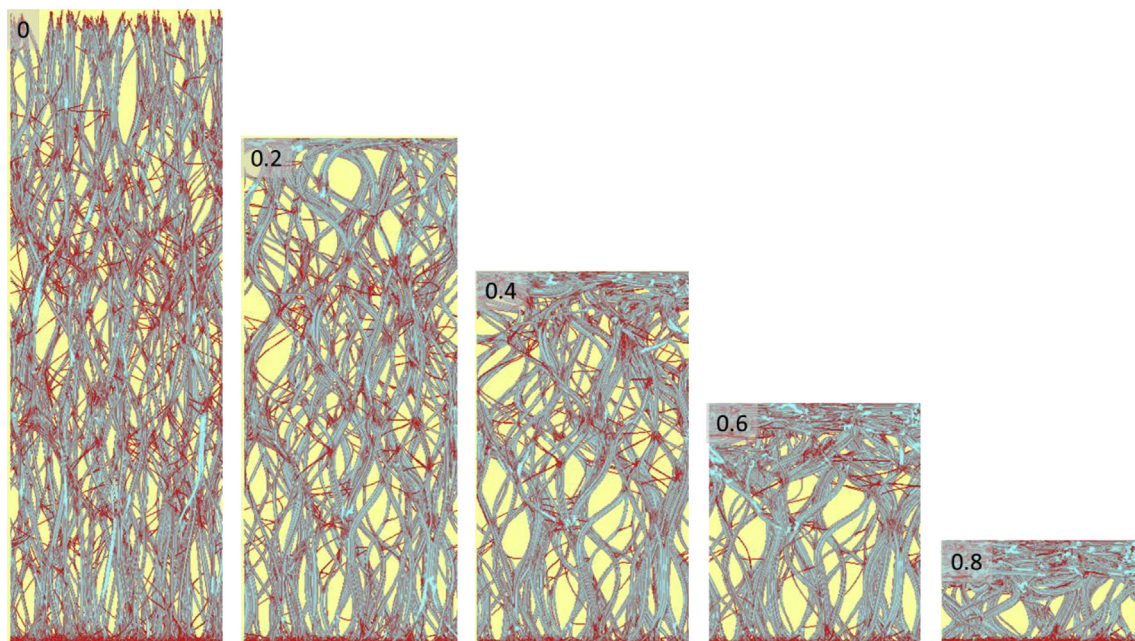


Fig. 1. Side view snapshots of the VACNT sample FA undergoing compressive deformation, with values of engineering strain ranging from 0 (initial undeformed sample) up to 0.8, as marked on the images. The two-tone coloring of CNT segments is by CNT-CNT interaction energy, where red corresponds to less favorable inter-tube interactions (isolated or almost isolated segments) and blue indicates more favorable interactions (nanotube segments integrated into CNT bundles). (A colour version of this figure can be viewed online.)

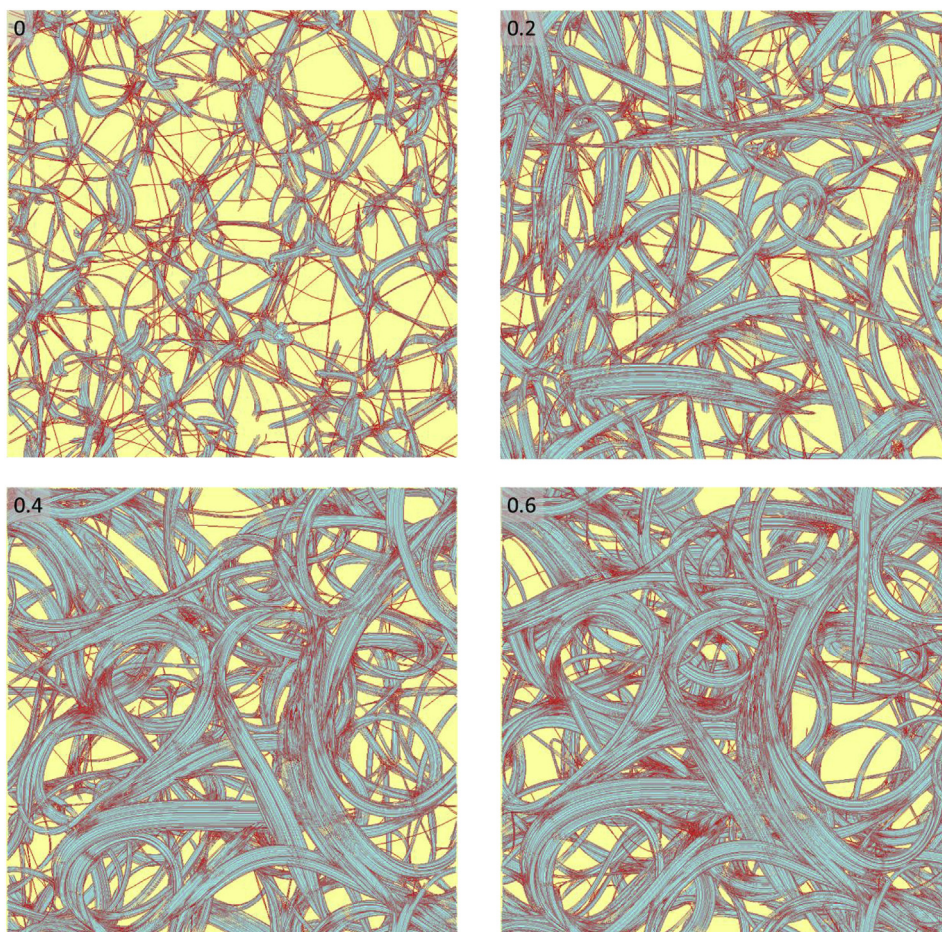


Fig. 2. Top-down view snapshots of the VACNT sample FA undergoing compressive deformation, with values of engineering strain ranging from 0 (initial undeformed sample) up to 0.6, as marked on the images. The two-tone coloring scheme is the same as in Fig. 1. The material in the bottom half of the sample height at the corresponding strain is blanked in order to more clearly show the evolution of the top layer. (A colour version of this figure can be viewed online.)

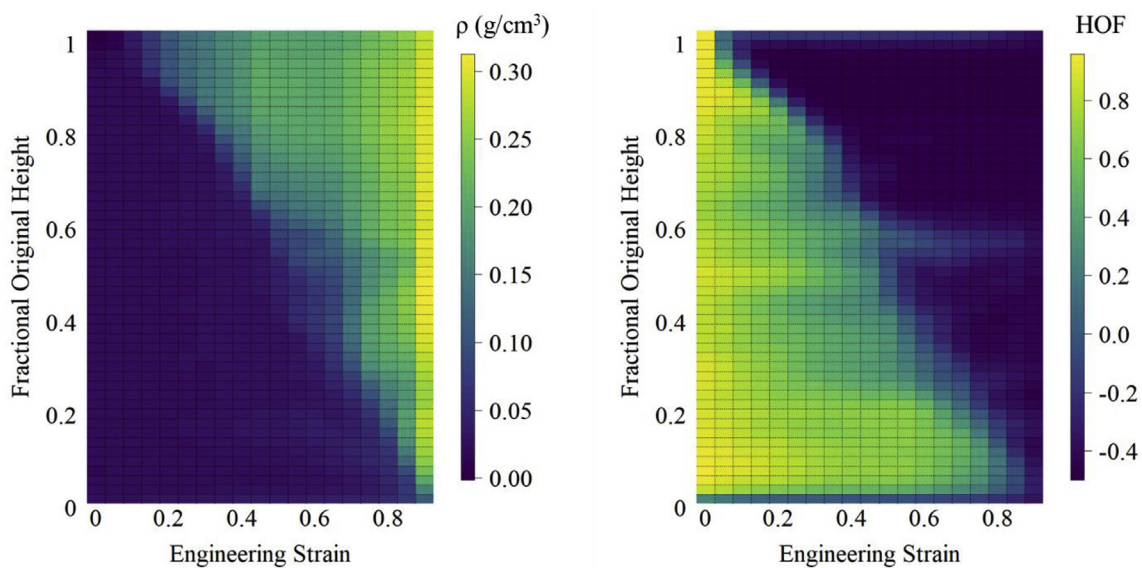


Fig. 3. Contour plots of the mass density ρ (a) and local HOF (b) calculated for VACNT sample FA by averaging over the sets of nanotube segments located in the same horizontal layers of the original uncompressed sample. The individual “pixels” in the plots correspond to strain increments by 0.05 (columns) and 40-nm-thick layers defined in the original sample (rows). (A colour version of this figure can be viewed online.)

course of the compressive deformation, the averaging done with the reference to the original location of the nanotube segments in the VACNT sample provides a more straightforward representation of the material redistribution between the two phases as compared to an alternative based on partitioning by the current positions of the segments in the deformed sample.

From the density contour plot shown in Fig. 3a, we see a clear picture of the emergence of a distinct densified region forming near the indenter. The rest of the forest remains largely unaffected by the densification and is separated from the dense region by a relatively well-defined interface that can already be identified at ~ 0.15 strain. With increasing strain, the top layer thickens and densifies in certain places beyond 0.2 g/cm^3 (ten times that of the initial forest density) at strains exceeding 0.4. Despite the theoretical maximum close-packed density of (10,10) SWCNTs being about 0.9 g/cm^3 , however, the density of the top layer does not increase beyond $\sim 0.23 \text{ g/cm}^3$ even at 0.7 strain, suggesting that constraints imposed on bundle reorganization prevent denser packing for this sample. Instead, the compressive deformation is accommodated by more material joining the dense-phase region with increasing strain. Note that the formation of densified regions under conditions of rapid deformation of VACNT forests [47–50] has been attributed in Ref. [48] to the formation of shock waves with anomalously slow, on the order of 10 m/s, shock front velocities. To address the possibility of the formation of a shock wave during the compression of sample FA, we performed a simulation where compression of the sample was stopped at 0.4 strain. The simulation was then continued with no additional deformation for additional 16 ns. As can be seen from Fig. S4 in the Supplementary Data, the interface separating the dense and rarified regions of the sample ceases to move with the absence of further deformation, thus indicating that the formation of the densified region in the simulation cannot be attributed to the shock wave formation.

The thickness of the interfacial layer separating the low- and high-density regions from each other remains relatively thin at low strains, spanning only a couple of hundreds of nanometers or less. At high strains exceeding ~ 0.5 , however, the interfacial layer becomes more diffuse. The decreased sharpness of the interface between the two regions can be attributed to the effect of the rigid boundary condition imposed on the bottom of the VACNT sample. The rigid attachment of the CNTs to the substrate starts to affect the ability of the CNT bundles to reorient themselves at the approaching interface with the dense region and makes the material to switch to alternative modes of compaction near the bottom of the forest. The compaction of the nanotubes attached to the substrate, however, requires a higher level of stresses, as can be seen from the stress – strain curve discussed below, which also produce a moderate increase in the density of the already compacted upper part of the sample up to $\sim 0.31 \text{ g/cm}^3$ at the maximum strain of 0.9 reached in the simulation.

As can be seen from Fig. 3b, the orientation of the CNTs also changes abruptly from the rarified phase, where the original vertical alignment of the nanotubes is largely retained and the local values of HOF remain in the range of 0.4–0.9, to the densified phase, where the nanotubes are reoriented parallel to the substrate and the local HOF becomes negative and stays below -0.4 in most of the densified phase. In contrast to density, which stays at almost the same level before the arrival of the densification front (Fig. 3a), the values of HOF visibly drop throughout the sample even at the early stage of the deformation process, at strains of 0.1–0.2. This drop is a reflection of a certain degree of bending deformation experienced by the vertically aligned CNT bundles in the low-density part of the sample. Nonetheless, there is still a clear demarcation in Fig. 3b between the horizontally oriented parts of the CNTs in the dense layer and those still in the rarified part of the

sample.

Another interesting feature in the HOF plot absent for density is the appearance of a stripe of elevated HOF at the fractional original height of ~ 0.55 . The non-monotonous variation of HOF along the height of the forest persists up to the maximum level of strain applied in the simulation and reflects the emergence of a collective mode of the forest deformation, i.e., on average, the segments in a certain cross-section of the sample have an orientation that is different from the one of in the surrounding material. To explain the origin of the local HOF maximum, we take note of five representative CNT shapes shown in Fig. 4a for sample FA at 0.6 strain. As expected, the top parts of the nanotubes are predominantly horizontally oriented, highly bent, and entangled into the dense region of the sample. Immediately below this region, however, the nanotubes are exhibiting large-scale zigzagging behavior that provides insights into the way the nanotubes transition from the low- to high-density phase.

Visually, the zigzagging of individual nanotubes in Fig. 4a shows some signs of collective coordinated behavior. This visual impression is supported by the results of the calculation of the distribution of HOF and parameter Δ characterizing the extent of the correlation in the lateral displacements of the nanotube segments along the height of the sample, shown in Fig. 4b. The parameter Δ is defined as $\Delta = \sqrt{\langle x - x_0 \rangle^2 + \langle y - y_0 \rangle^2}$, where x and y are the positions of the nodes at a given strain, x_0 and y_0 are the positions of the same nodes in the original sample, and the angled brackets $\langle \rangle$ denote averaging over all CNT segments in a given layer of the forest.

The local maxima in the distributions of HOF and Δ around a height of $0.62 \mu\text{m}$ (marked by the upper dashed line in Fig. 4b) coincide with the location of the local minimum in the density plot, as well as with the stripe of elevated HOF at the fractional original height of ~ 0.55 in the contour plot shown in Fig. 3b. The emergence of another similar oscillation in Δ and HOF can be seen in the lower part of the VACNT forest, at around $0.5 \mu\text{m}$, Fig. 4b, and can be related to the pronounced bowing seen for the individual CNTs in the snapshot shown in Fig. 4a. All these correlations are consistent with the physical picture of collective folding of the nanotubes in the vicinity of the advancing densification front. Indeed, the collective folding localized within a VACNT forest cross-section is expected to produce alternating regions of densely-packed horizontally aligned nanotubes (local maxima of ρ and minima of HOF) and lower density regions with higher degree of vertical orientation of CNT segments (local maxima of HOF and Δ , and minima of ρ) around the vertexes of the folds.

The degree of correlation in the lateral displacements of nanotubes near the advancing densification front, however, does not allow us to directly associate the zigzagging/folding of the CNTs observed in the simulation to the phenomenon of coordinated buckling reported in some of the experimental studies [3,6,7,10,14,24]. The relatively small height of the simulated forest ($2 \mu\text{m}$) and the high flexibility of SWCNTs, which enables alternative modes of bending deformation [51] and folding into the compact horizontally aligned structure, prevent the occurrence of well-defined periodic coordinated buckling across the sample cross-section. Indeed, it has been noted in Ref. [24] that buckling becomes highly periodic for multi-walled carbon nanotube (MWCNT) forests that are taller than $190 \mu\text{m}$, and the typical period between successive buckling kinks ranges between 3 and $6 \mu\text{m}$, although a single coordinated buckling event is still observed for forests as short as $35 \mu\text{m}$. Nevertheless, the coordinated local bowing and displacement of SWCNTs leading to the folding into high-density phase, observed in the simulation, can be considered to be a potential precursor for the more ordered periodic coordinated buckling that produces discrete regions of stacked densified

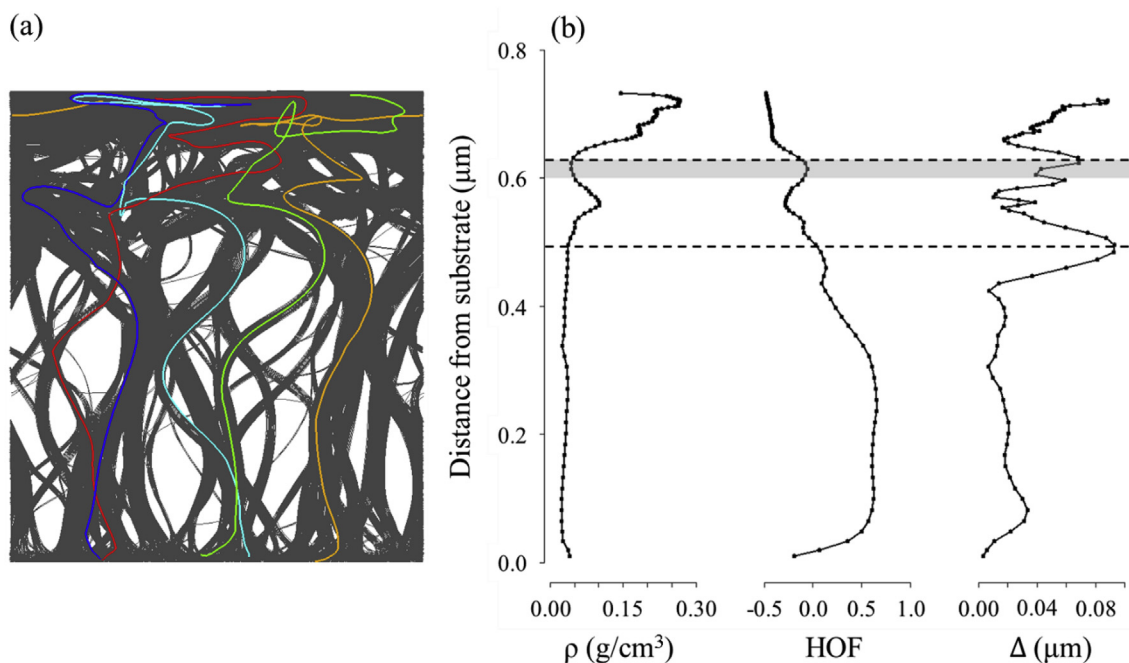


Fig. 4. Snapshot of sample FA compressed to 0.6 strain with an overlay of five representative CNTs shown in different colors (a), and plots of the variation of density ρ , HOF, and parameter Δ characterizing the extent of the correlation in the lateral displacements of the nanotube segments along the height of the forest (b). The dashed lines in (b) mark the locations of the two HOF local maxima and the gray stripe marks the height that corresponds to the local HOF maxima at strain 0.6 in the contour plot shown in Fig. 3b. Each data point in (b) corresponds to averaging over a layer that contains 1% of the total mass of the VACNT forest. The evolution of the shapes of the five nanotubes highlighted in (a) during the deformation can be followed in Fig. S5 in the Supplementary Data, where the snapshots are shown for strain increments of 0.2. (A colour version of this figure can be viewed online.)

layers upon the compressive deformation of taller forests consisting of more rigid MWCNTs [3,6,7,10,14].

The connection between the collective nature of the nanotube bending deformation in the simulations and the experimentally observed periodic collective buckling is also supported by the non-monotonous variation of stress with increasing engineering strain shown for the computational sample FA in Fig. 5a. Experimentally, a coordinated buckling across a forest cross-section is mechanically registered as an undulation on the plateau part of the stress-strain dependence [6,7,10,14]. The coordinated buckling relieves some of the stress exerted by the forest on the indenter, resulting in a dip in the stress-strain curve.

To reveal the underlying physical reasons behind the localization of the deformation process within the relatively narrow and

well-defined interfacial region separating the dense and rarefied parts of the VACNT forest, we now turn to the analysis of the energy evolution in the forest during the deformation. We focus our attention on the inter-tube interaction energy and nanotube bending energy that account for $\sim 99\%$ of the energy change during the compressive deformation up to 0.9 strain. The evolution of these two major contributions to the total energy of a VACNT forest is shown in Fig. 6, where both the energy in the whole sample FA, and the distribution of the energy with respect to the original height of the nanotube segments (same representation as the one used in Fig. 3) are presented in Fig. 6ab and Fig. 6cd, respectively.

It is clear that the phase separation observed in the course of the deformation is an energetically favorable process for sample FA, as the rise in the bending energy (Fig. 6b) is more than offset by the

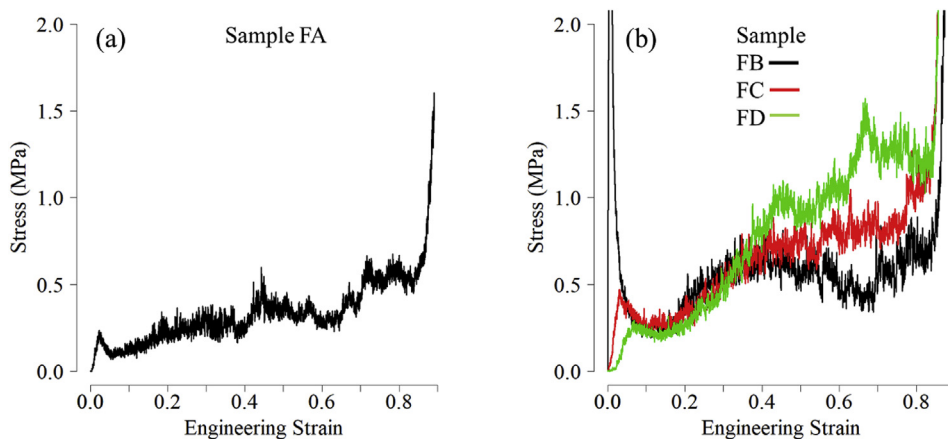


Fig. 5. Stress-strain response of 2- μm -tall sample FA (a) and 0.6- μm -tall samples FB, FC, and FD (b) compressed at an indenter velocity of 50 m/s to 0.9 engineering strain. (A colour version of this figure can be viewed online.)

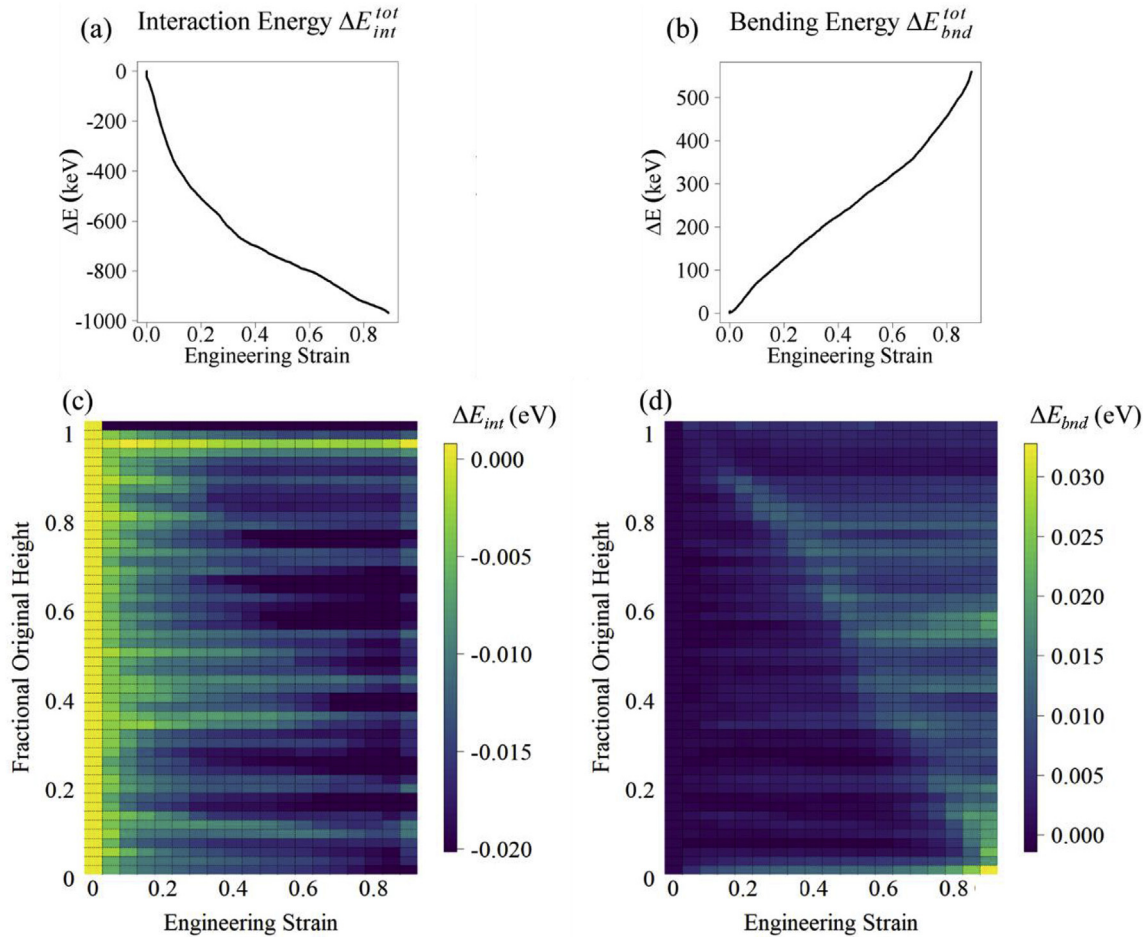


Fig. 6. The evolution of the inter-tube interaction energy ΔE_{int} (a,c) and nanotube bending energy ΔE_{bnd} (b,d) during the compressive deformation of sample FA up to a maximum engineering strain of 0.9. The total energies for the whole sample FA, ΔE_{int}^{tot} and ΔE_{bnd}^{tot} , are shown in (a,b), and the distributions of the energies with respect to the original height of the nanotube segments in the uncompressed sample are presented in (c,d). The individual “pixels” in (c,d) correspond to strain increments by 0.05 (columns) and 40-nm-thick layers defined in the original sample (rows). (A colour version of this figure can be viewed online.)

decrease in CNT-CNT interaction energy (Fig. 6a). The decrease in the inter-tube interaction energy is not limited to the part of the VACNT forest undergoing the densification, where the nanotubes self-organize into energetically favorable arrangements of thick CNT bundles, but also extends to the lower rarified part of the sample, reflecting the bundle coarsening and corresponding decrease in the inter-tube interaction energy, Fig. 6c.

The transition between the two phases is even more apparent in the distribution of the bending energy shown in Fig. 6d, where the densification is associated with energy increase. Interestingly, the energy increase is the largest in the interfacial region, and the bending energy is reduced to a certain degree inside the densified part of the sample, as can be seen from the local energy maximum along the propagating densification front in Fig. 6d. The local increase in the bending energy in the interfacial region is expected from the visual picture of the nanotube bending and folding during the transformation from the rarified vertically oriented phase to the dense horizontally oriented phase discussed above. The elevated energy of the interfacial region also presents an energy barrier preventing the spontaneous collapse of the VACNT forest into the lower-energy densified phase. Nevertheless, the decrease of the total energy of the forest upon the compression suggests that the compressed phase should be stable after the indenter is removed. Although we do not test this due to the high computational expense of the large-scale simulation of the slow structural changes

upon the unloading of sample FA, a substantial irreversible (plastic) deformation has been observed in earlier smaller-scale simulations performed for 0.2- μm -tall SWCNT forests repeatedly loaded and unloaded to 0.6 and 0.8 strain [8]. Forests composed of MWCNTs with large diameters, however, are more likely to elastically deform [52] due to the high bending modulus of the MWCNTs [53–55] and the correspondingly larger contribution of the increase in the bending energy to the total energy cost of the compressive deformation of the VACNT forests.

Note that while in the simulation discussed above the nucleation of the dense phase is observed in the top part of the sample, in the direct vicinity of the indenter, the experiments reveal the appearance of the densified phase either (or both) at the top (near the indenter) and/or bottom (near the substrate) of the CNT forest [3,6,7,10–15,24]. The locations of the nucleation sites in experiments correspond to zones of weakest flexural rigidity of the VACNT forest, which are defined by multiple factors, including uneven distribution of defects, density gradients, variable degree of alignment of CNT bundles, or structural heterogeneities introduced in the growth process. In particular, the coordinated buckling often starts near the base of the forest, where the density can be lowest [6,7,13,14], and CNT diameter may be smaller due to shrinkage of catalytic particles during the nanotube growth process [11,52]. The computational sample used in the simulation does not have such types of preferential nucleation sites, and the natural location of the

appearance of the densified phase is near the indenter, where the ends of the nanotubes have more freedom to slide along the indenter and assemble into a dense phase composed of horizontally oriented thick CNT bundles. Once a region of the dense phase is formed, however, its further growth is no longer controlled by the presence of the indenter or the free ends of the nanotubes, which are now immobilized by the entanglement into the dense phase.

4. Effect of forest structure and length on the deformation mechanism

In order to verify that the mechanism of the compressive deformation revealed in the simulation reported above for sample FA is general and is activated in samples with different microstructures, we perform an additional set of simulations for VACNT forest samples FB, FC, and FD, which have the same density of 0.02 g/cm^3 but different structural characteristics (*i.e.*, thickness of the bundles and CNT inclination, as can be seen from Table 1 and Figs. S2b–d in the Supplementary Data). The lateral size of the computational cell used in these simulations is close to that of sample FA ($0.6 \mu\text{m}$ compared to $0.641 \mu\text{m}$ for FA), but the length of the forest is reduced to $0.6 \mu\text{m}$. The use of the shorter forests reduces the computational cost of the simulations and, at the same time, allows us to explore the effect of nanotube length on the deformation behavior by relating the results of the simulations to those discussed above for the longer $2\text{-}\mu\text{m}$ -tall sample FA and those reported in Ref. [8] for shorter $0.2\text{-}\mu\text{m}$ -tall forests.

The snapshots of samples FB, FC, and FD taken at different stages of the compressive deformation, Fig. 7, reveal the mechanical response visually similar to that observed for the longer forest in Fig. 1. In all samples, we see the formation of a densified layer near the indenter at the early stage of the deformation process, followed by gradual thickening of the densified layer. In comparison with the taller sample FA, however, there is less pronounced localization of the bending deformation within the interfacial region, and no signs of the collective folding of CNT bundles in the vicinity of the densified region. Rather, at higher strains, the CNT bundles tend to bow sidewise or bent into serpentine shapes along much of the height of the forest, particularly in the case of samples FB and FC composed of thicker and less entangled bundles. Overall, the deformation of the $0.6\text{-}\mu\text{m}$ -tall CNT forests exhibits intermediate characteristics between those observed for shorter $0.2\text{-}\mu\text{m}$ -tall forests [8], where the mechanical response is dominated by the deformation of individual bundles that either bow or fold at their bases, and those discussed above for taller sample FA, where the deformation process is largely localized within the interfacial region separating the distinct rarified and dense phases of the material. The greater bundle entanglement in sample FD makes it difficult for CNT bundles to move independently from one another, leading to a less localized material response to the deformation.

The distributions of density and HOF along the fractional original height, shown in Fig. 8 for samples FB, FC, and FD compressed to 0.6 strain, suggest that the deformation mechanism of these shorter forests is the same as the one discussed in section 3 for the $2\text{-}\mu\text{m}$ -tall sample FA. Both the density and HOF distributions exhibit a relatively sharp transition from the low- to high-density phases characterized by vertical and horizontal preferential alignment of nanotube segments, respectively. In contrast to the taller forest, however, the variation of density and HOF in the interfacial region separating the two phases is smooth and does not display the intermediate oscillations observed in Fig. 4b for sample FA. As discussed in section 3, these oscillations are caused by the collective zigzagging and folding of the CNT bundles involved in the phase transition in the taller sample. For the shorter samples, these processes are inhibited by the global rearrangement of CNT bundles

in response to the mechanical deformation, which helps to accommodate the transition of nanotube segments into the high-density horizontally aligned phase without the activation of the localized folding deformation.

Stress-strain curves, plotted for samples FB, FC, and FD in Fig. 5b, exhibit the same general three-stage response to the uniaxial compression that has been observed for the taller sample FA (section 3) as well as for real VACNT forests [6,7]. The magnitude of stresses is somewhat higher for the shorter forests in the whole range of strains (*e.g.*, compare the curve for sample FA in Fig. 5a with the one of sample FC, which has the same average inclination of nanotube segments, see Table 1). The elevated level of stresses is related to the transition from the more localized deformation of the nanotubes in the interfacial region in the case of tall forests to the more global response of the whole CNT bundles to the deformation of shorter forests, which becomes even more pronounced with further shortening of the nanotubes [8].

Comparing the $0.6\text{-}\mu\text{m}$ -tall samples with each other (Fig. 5b), we see that the first stress peak is most prominent for sample FB and comes from the axial compression of its highly oriented CNT bundles. The forests where the CNT bundles have a higher inclination with respect to the vertical axis (as quantified by values of HOF listed in Table 1) exhibit a much more muted initial stress response to the deformation. Following the initial peak, the extended plateau stress stage sets up and extends up to strains of ~ 0.85 . Due to the greater degree of entanglement limiting mobility of bundles and their ability to reorganize themselves in the optimal way to reduce stress, the average stress increases from FB to FC to FD starting from strains of ~ 0.45 . At a qualitative level, this observation may be related to a model suggested in Ref. [56], where a simplified description of interconnections between the bundles was introduced and related to the ability of VACNT forests to support the lateral force transfer required for their “drawability.” Finally, above 0.85 strain, the densification regime is heralded by a sharp increase in stress observed for all samples. At this point, the CNTs have limited ability to reorganize themselves to release stress, and increasing strain will see the entire forest converted to the densified phase. Overall, despite the substantial quantitative effect of the height and structural organization of VACNT forests on their mechanical behavior, we can conclude that the general picture of the compressive deformation proceeding through the phase transformation from a low-density vertically aligned phase to a high-density phase characterized by horizontal alignment of nanotubes holds for VACNT forests of various structural organization and height exceeding several hundreds of nanometers.

5. Summary

The mechanical response of VACNT forests undergoing extensive compressive deformation is investigated in large-scale mesoscopic simulations of the uniaxial compression of a VACNT forest composed of $2\text{-}\mu\text{m}$ -long SWCNTs as well as three structurally distinct forests composed of $0.6\text{-}\mu\text{m}$ -long SWCNTs. The simulations reveal that the compressive deformation proceeds as a phase transformation from an original low-density phase composed of vertically aligned CNT bundles to a densified phase characterized by horizontal preferential alignment of nanotube segments. The two phases are separated by a well-defined interfacial layer, which advances during the compressive deformation through localized bending and folding of nanotube segments. For the $2\text{-}\mu\text{m}$ -tall forest, the nanotube folding involves correlated displacement of multiple CNT bundles across the lateral extent of the computational cell, hinting on the origin of the collective buckling behavior observed experimentally for even taller VACNT forests composed of stiffer MWCNTs.

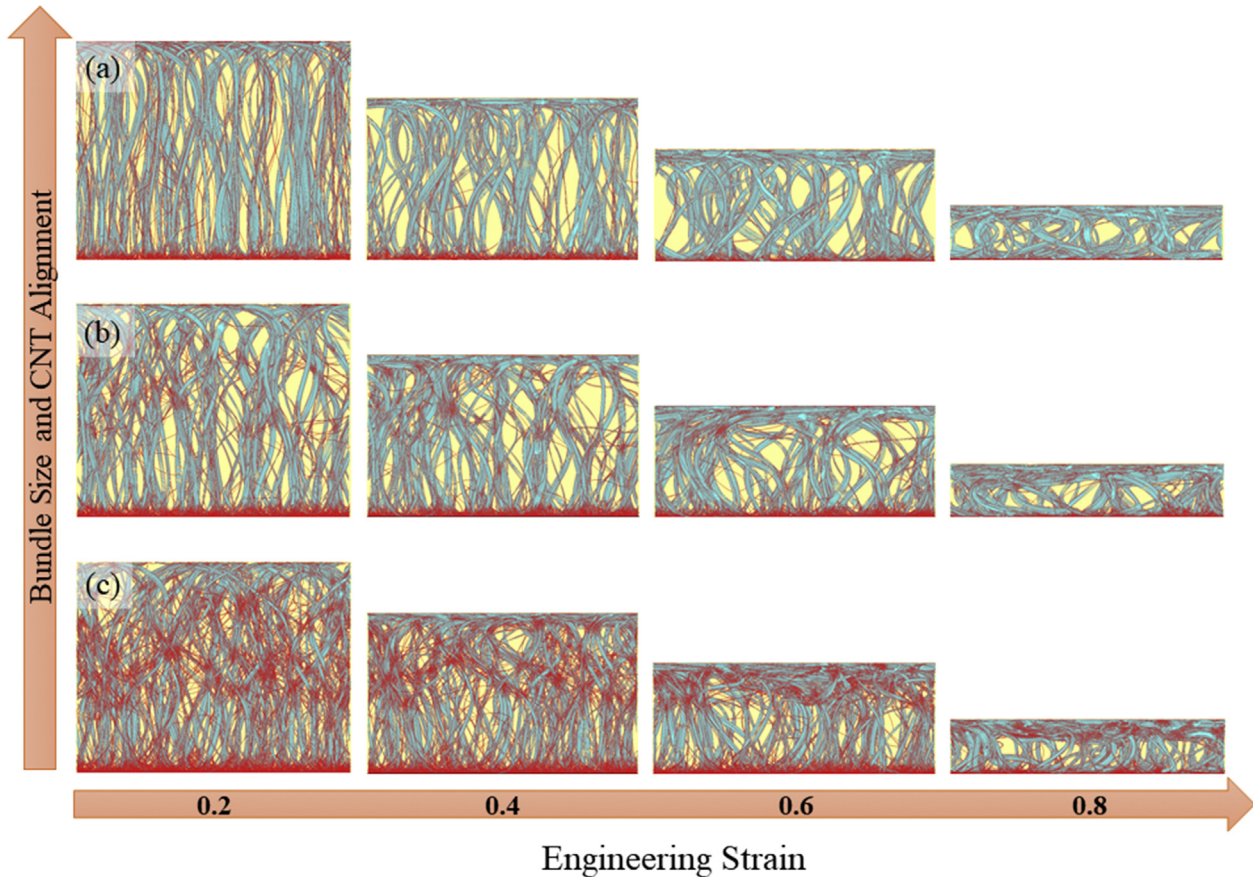


Fig. 7. Side views snapshots of the VACNT samples FB (a), FC (b), and FD (c) undergoing compressive deformation, with values of engineering strain marked at the bottom. The two-tone coloring scheme is the same as in Fig. 1. (A colour version of this figure can be viewed online.)

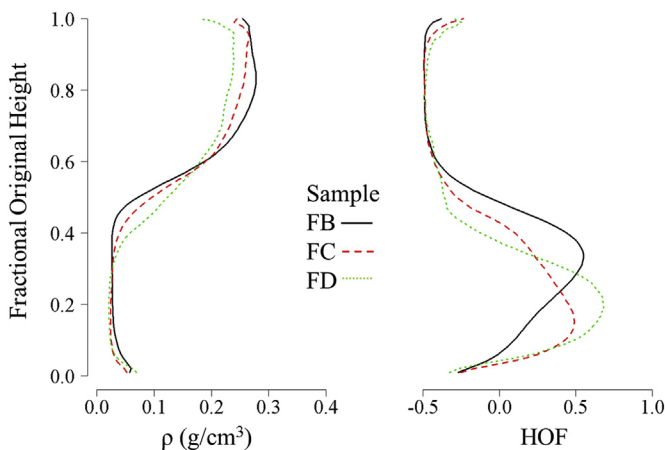


Fig. 8. The distributions of density and HOF along the fractional original height of the forest for samples FB, FC, and FD compressed to an engineering strain of 0.6. (A colour version of this figure can be viewed online.)

While the initial realignment of CNTs at the start of the deformation process is triggered by the interaction with the indenter, further growth of the dense region is driven by the energy minimization. The bending energy of the nanotube segments joining the densified phase in the course of the compressive deformation increases, but the reduction of the inter-tube van der Waals interaction energy more than compensates for this extra bending deformation energy. The decrease in the total energy suggests that

the deformation of the forests consisting of highly flexible SWCNTs has a large irreversible/plastic component. The localized bending deformation associated with reorientation of nanotube segments upon the transition from the rarified vertically oriented phase to the dense horizontally oriented phase results in the local maximum of the bending energy, which serves as a barrier preventing the spontaneous collapse of the VACNT forest into the lower-energy densified phase. The higher bending stiffness of MWCNTs is likely to shift the energy balance in favor of the positive contribution of the bending energy, making the recovery energetically favorable. The characteristic three-stage stress-strain dependence (an initial "elastic" peak followed by an extended plateau region and a sharp rise of stress in the densification regime), commonly observed in the experimental probing of mechanical properties of VACNT forests, is reproduced in all of the simulations, suggesting that the heterogeneous propagation of densification front is the general mechanism of the mechanical deformation of VACNT forests.

Acknowledgements

Financial support for this work is provided by the National Aeronautics and Space Administration through an Early Stage Innovations grant from NASA's Space Technology Research Grants Program (NNX16AD99G). Computational support is provided by the National Science Foundation through the Extreme Science and Engineering Discovery Environment (Project CTS160026) and by NASA's Advanced Supercomputing (NAS) Division.

Appendix A. Supplementary data

Supplementary data to this article can be found online at <https://doi.org/10.1016/j.carbon.2018.11.066>.

References

- [1] E.G. Rakov, Materials made of carbon nanotubes. The carbon nanotube forest, *Russ. Chem. Rev.* 82 (6) (2013) 538–566.
- [2] M.F. Ashby, The properties of foams and lattices, *Philos. T. R. Soc. A* 364 (1838) (2006) 15–30.
- [3] A. Cao, P.L. Dickrell, W.G. Sawyer, M.N. Ghasemi-Nejhad, P.M. Ajayan, Supercompressible foamlite carbon nanotube films, *Science* 310 (5752) (2005) 1307–1310.
- [4] J. Suhr, P. Victor, L. Ci, S. Sreekala, X. Zhang, O. Nalamasu, P.M. Ajayan, Fatigue resistance of aligned carbon nanotube arrays under cyclic compression, *Nat. Nanotechnol.* 2 (7) (2007) 417–421.
- [5] E.H.T. Teo, W.K.P. Yung, D.H.C. Chua, B.K. Tay, A carbon nanomattress: a new nanosystem with intrinsic, tunable, damping properties, *Adv. Mater.* 19 (19) (2007) 2941–2945.
- [6] S.B. Hutchens, L.J. Hall, J.R. Greer, In situ mechanical testing reveals periodic buckle nucleation and propagation in carbon nanotube bundles, *Adv. Funct. Mater.* 20 (14) (2010) 2338–2346.
- [7] S. Pathak, E.J. Lim, P.P. Abadi, S. Graham, B.A. Cola, J.R. Greer, Higher recovery and better energy dissipation at faster strain rates in carbon nanotube bundles: an in-situ study, *ACS Nano* 6 (3) (2012) 2189–2197.
- [8] B.K. Wittmaack, A.N. Volkov, L.V. Zhigilei, Mesoscopic modeling of the uniaxial compression and recovery of vertically aligned carbon nanotube forests, *Compos. Sci. Technol.* 166 (2018) 66–85.
- [9] V.S. Deshpande, M.F. Ashby, N.A. Fleck, Foam topology bending versus stretching dominated architectures, *Acta Mater.* 49 (6) (2001) 1035–1040.
- [10] A.A. Zbib, S.D. Mesarovic, E.T. Lilleodden, D. McClain, J. Jiao, D.F. Bahr, The coordinated buckling of carbon nanotube turfs under uniform compression, *Nanotechnology* 19 (17) (2008) 175704.
- [11] Y. Li, H.-i. Kim, B. Wei, J. Kang, J.-b. Choi, J.-D. Nam, J. Suhr, Understanding the nanoscale local buckling behavior of vertically aligned MWCNT arrays with van der Waals interactions, *Nanoscale* 7 (34) (2015) 14299–14304.
- [12] S. Pathak, N. Mohan, P.P.S.S. Abadi, S. Graham, B.A. Cola, J.R. Greer, Compressive response of vertically aligned carbon nanotube films gleaned from in situ flat-punch indentations, *J. Mater. Res.* 28 (7) (2013) 984–997.
- [13] S.B. Hutchens, A. Needleman, J.R. Greer, Analysis of uniaxial compression of vertically aligned carbon nanotubes, *J. Mech. Phys. Solid.* 59 (10) (2011) 2227–2237.
- [14] S. Pathak, N. Mohan, E. Decolvenaere, A. Needleman, M. Bedewy, A.J. Hart, J.R. Greer, Local relative density modulates failure and strength in vertically aligned carbon nanotubes, *ACS Nano* 7 (10) (2013) 8593–8604.
- [15] M.R. Maschmann, Q. Zhang, R. Wheeler, F. Du, L. Dai, J. Baur, In situ SEM observation of column-like and foam-like CNT array nanoindentation, *ACS Appl. Mater. Interfaces* 3 (3) (2011) 648–653.
- [16] F. Fraternali, T. Blesgen, A. Amendola, C. Daraio, Multiscale mass-spring models of carbon nanotube foams, *J. Mech. Phys. Solid.* 59 (1) (2011) 89–102.
- [17] T. Blesgen, F. Fraternali, J.R. Raney, A. Amendola, C. Daraio, Continuum limits of bistable spring models of carbon nanotube arrays accounting for material damage, *Mech. Res. Commun.* 45 (2012) 58–63.
- [18] X.J. Liang, J.H. Shin, D. Magagnosc, Y.J. Jiang, S.J. Park, A.J. Hart, K. Turner, D.S. Gianola, P.K. Purohit, Compression and recovery of carbon nanotube forests described as a phase transition, *Int. J. Solid Struct.* 122 (2017) 196–209.
- [19] G. Puglisi, L. Truskinovsky, Mechanics of a discrete chain with bi-stable elements, *J. Mech. Phys. Solid.* 48 (1) (2000) 1–27.
- [20] G. Puglisi, L. Truskinovsky, Rate independent hysteresis in a bi-stable chain, *J. Mech. Phys. Solid.* 50 (2) (2002) 165–187.
- [21] G. Puglisi, L. Truskinovsky, Thermodynamics of rate-independent plasticity, *J. Mech. Phys. Solid.* 53 (3) (2005) 655–679.
- [22] O.V. Kim, R.I. Litvinov, J.W. Weisel, M.S. Alber, Structural basis for the nonlinear mechanics of fibrin networks under compression, *Biomaterials* 35 (25) (2014) 6739–6749.
- [23] O.V. Kim, X. Liang, R.I. Litvinov, J.W. Weisel, M.S. Alber, P.K. Purohit, Foam-like compression behavior of fibrin networks, *Biomechanics Model. Mechanobiol.* 15 (1) (2016) 213–228.
- [24] M.R. Maschmann, Q.H. Zhang, F. Du, L.M. Dai, J. Baur, Length dependent foam-like mechanical response of axially indented vertically oriented carbon nanotube arrays, *Carbon* 49 (2) (2011) 386–397.
- [25] L.V. Zhigilei, C. Wei, D. Srivastava, Mesoscopic model for dynamic simulations of carbon nanotubes, *Phys. Rev. B* 71 (16) (2005) 165417.
- [26] A.N. Volkov, L.V. Zhigilei, Mesoscopic interaction potential for carbon nanotubes of arbitrary length and orientation, *J. Phys. Chem. C* 114 (12) (2010) 5513–5531.
- [27] M.J. Buehler, Mesoscale modeling of mechanics of carbon nanotubes: self-assembly, self-folding, and fracture, *J. Mater. Res.* 21 (11) (2006) 2855–2869.
- [28] I. Ostanin, R. Ballarini, D. Potyondy, T. Dumitrică, A distinct element method for large scale simulations of carbon nanotube assemblies, *J. Mech. Phys. Solid.* 61 (3) (2013) 762–782.
- [29] B.K. Wittmaack, A.H. Banna, A.N. Volkov, L.V. Zhigilei, Mesoscopic modeling of structural self-organization of carbon nanotubes into vertically aligned networks of nanotube bundles, *Carbon* 130 (2018) 69–86.
- [30] A.N. Volkov, T. Shiga, D. Nicholson, J. Shiomi, L.V. Zhigilei, Effect of bending buckling of carbon nanotubes on thermal conductivity of carbon nanotube materials, *J. Appl. Phys.* 111 (5) (2012), 053501.
- [31] K.M. Liew, X.Q. He, C.H. Wong, On the study of elastic and plastic properties of multi-walled carbon nanotubes under axial tension using molecular dynamics simulation, *Acta Mater.* 52 (9) (2004) 2521–2527.
- [32] S. Iijima, C. Brabec, A. Maiti, J. Bernholc, Structural flexibility of carbon nanotubes, *J. Chem. Phys.* 104 (5) (1996) 2089–2092.
- [33] B. Bhushan, Nanotribology of carbon nanotubes, *J. Phys. Condens. Matter* 20 (36) (2008) 365214.
- [34] O. Suekane, A. Nagataki, H. Mori, Y. Nakayama, Static friction force of carbon nanotube surfaces, *Appl. Phys. Express* 1 (6) (2008) 064001.
- [35] S. Akita, Y. Nakayama, Interlayer sliding force of individual multiwall carbon nanotubes, *Jpn. J. Appl. Phys.* 42 (7S) (2003) 4830–4833.
- [36] J. Cumings, A. Zettl, Low-friction nanoscale linear bearing realized from multiwall carbon nanotubes, *Science* 289 (5479) (2000) 602.
- [37] T. Filletter, S. Yockel, M. Naraghi, J.T. Paci, O.C. Compton, M.L. Mayes, S.T. Nguyen, G.C. Schatz, H.D. Espinosa, Experimental-computational study of shear interactions within double-walled carbon nanotube bundles, *Nano Lett.* 12 (2) (2012) 732–742.
- [38] J.T. Paci, A. Furmanchuk, H.D. Espinosa, G.C. Schatz, Shear and friction between carbon nanotubes in bundles and yarns, *Nano Lett.* 14 (11) (2014) 6138–6147.
- [39] G.F. Zhong, T. Iwasaki, H. Kawarada, Semi-quantitative study on the fabrication of densely packed and vertically aligned single-walled carbon nanotubes, *Carbon* 44 (10) (2006) 2009–2014.
- [40] G.F. Zhong, J.H. Warner, M. Fouquet, A.W. Robertson, B.A. Chen, J. Robertson, Growth of ultrahigh density single-walled carbon nanotube forests by improved catalyst design, *ACS Nano* 6 (4) (2012) 2893–2903.
- [41] D.N. Futaba, K. Hata, T. Yamada, T. Hiraoka, Y. Hayamizu, Y. Kakudate, O. Tanaike, H. Hatori, M. Yumura, S. Iijima, Shape-engineerable and highly densely packed single-walled carbon nanotubes and their application as super-capacitor electrodes, *Nat. Mater.* 5 (12) (2006) 987–994.
- [42] E. Einarsson, H. Shiozawa, C. Kramberger, M.H. Rummeli, A. Gruneis, T. Pichler, S. Maruyama, Revealing the small-bundle internal structure of vertically aligned single-walled carbon nanotube films, *J. Phys. Chem. C* 111 (48) (2007) 17861–17864.
- [43] S.J. Kang, C. Kocabas, T. Ozel, M. Shim, N. Pimparkar, M.A. Alam, S.V. Rotkin, J.A. Rogers, High-performance electronics using dense, perfectly aligned arrays of single-walled carbon nanotubes, *Nat. Nanotechnol.* 2 (4) (2007) 230–236.
- [44] G.H. Chen, Y. Seki, H. Kimura, S. Sakurai, M. Yumura, K. Hata, D.N. Futaba, Diameter control of single-walled carbon nanotube forests from 1.3–3.0 nm by arc plasma deposition, *Sci. Rep.* 4 (2014) 3804.
- [45] Information about the Comet supercomputer can be found by visiting. <https://portal.xsede.org/sdsc-comet>.
- [46] H.J. Berendsen, J.P.M. Postma, W.F. Vangunsteren, A. Dinola, J.R. Haak, Molecular dynamics with coupling to an external bath, *J. Chem. Phys.* 81 (8) (1984) 3684–3690.
- [47] C. Daraio, V.F. Nesterenko, S. Jin, W. Wang, A.M. Rao, Impact response by a foamlite forest of coiled carbon nanotubes, *J. Appl. Phys.* 100 (6) (2006) 064309.
- [48] R. Thevamaran, E.R. Meshot, C. Daraio, Shock formation and rate effects in impacted carbon nanotube foams, *Carbon* 84 (2015) 390–398.
- [49] R. Thevamaran, F. Fraternali, C. Daraio, Multiscale mass-spring model for high-rate compression of vertically aligned carbon nanotube foams, *J. Appl. Mech.* 81 (12) (2014) 121006.
- [50] A. Misra, J.R. Greer, C. Daraio, Strain rate effects in the mechanical response of polymer-anchored carbon nanotube foams, *Adv. Mater.* 21 (3) (2009) 334–338.
- [51] R. Richards Jr., Principles of Solid Mechanics, CRC Press, New York, 2000.
- [52] O. Yagliglu, A.Y. Cao, A.J. Hart, R. Martens, A.H. Slocum, Wide range control of microstructure and mechanical properties of carbon nanotube forests: a comparison between fixed and floating catalyst CVD techniques, *Adv. Funct. Mater.* 22 (23) (2012) 5028–5037.
- [53] I. Nikiforov, D.B. Zhang, R.D. James, T. Dumitrică, Wavelike rippling in multi-walled carbon nanotubes under pure bending, *Appl. Phys. Lett.* 96 (12) (2010) 123107.
- [54] H. Jackman, P. Krakhmalev, K. Svensson, Mechanical behavior of carbon nanotubes in the rippled and buckled phase, *J. Appl. Phys.* 117 (8) (2015) 084318.
- [55] C.G. Wang, Y.P. Liu, J. Al-Ghalith, T. Dumitrică, M.K. Wadee, H.F. Tan, Buckling behavior of carbon nanotubes under bending: from ripple to kink, *Carbon* 102 (2016) 224–235.
- [56] A.A. Kuznetsov, A.F. Fonseca, R.H. Baughman, A.A. Zakhidov, Structural model for dry-drawing of sheets and yarns from carbon nanotube forests, *ACS Nano* 5 (2) (2011) 985–993.